Ultrafast Mode Reversal Coriolis Gyroscopes

Yuchen Wang, *Member, IEEE*, Jiakun Hou, Chong Li, *Member, IEEE*, Jin Wu, *Member, IEEE*, Yu Jiang, *Member, IEEE*, Ming Liu, *Senior Member, IEEE*, and John Y. Hung, *Fellow, IEEE*

***Abstract*—Mode reversal is an advanced technique that can effectively improve the performance of the Coriolis vibratory gyros (CVGs). In this article, we propose and demonstrate a modified mode reversal scheme to reduce the measurement dead zone limitations of state-of-the-art mode switching in CVGs. The dynamic model and working principle of the mode reversal gyro are first reviewed. Theoretical analysis and experimental verification are conducted to describe nonlinearity, mode coupling, and time-varying characteristics. A reversal scheme based on iterative learning control (ILC) is then presented. The experimental results showed 145% improvement in reversal speed and 90% reduction in overshoot when compared to other popular controllers and robustness to environmental variations.**

***Index Terms*—Coriolis vibratory gyroscopes (CVGs), hemispherical resonator gyroscopes (HRGs), inertial sensors, MEMS gyroscopes, mode reversal gyroscopes.**

I. Introduction

CORIOLIS vibratory gyroscopes (CVGs) are inertial sensors broadly applied in applications such as automobiles, game controllers, smartphones, radio-controlled hobby vehicles, industrial robotics, and camera image stabilization systems [1], [2]. The Segway human transporter control system was stabilized by a set of CVGs. CVGs are mainly divided into microelectromechanical systems (MEMS) gyroscopes and hemispherical resonant gyroscopes (HRGs), but all share the same fundamental operation principle based on the Coriolis effect for angular rate measurements. Comparing the two types, the former has the advantages of smaller size, lower cost, and lower power consumption [3], [4], while the latter has a higher quality factor and measurement accuracy [5].

However, CVGs suffer from the famous bias instability problem, which is induced by inherent manufacturing inaccuracies as well as environmental influences [6], [7]. Bias instability is the core performance index of gyroscopes, which reflects the stability of the bias in a period of time through the Allan variance. Many works toward this fatal issue have been presented and demonstrated. Methods to enhance robustness and scale factor include vacuum packages, improved manufacturing process, special mechanical materials, and electronics calibration methods [8], [9]. The mode reversal operation scheme is an advanced solution that can effectively improve the bias instability. The principle of mode reversal is to periodically switch between the two gyroscopic modes to maintain the symmetry of the mechanical part [10], [11].

As a tradeoff, there would be a measurement dead zone during switching processes to interfere the normal operation. Therefore, two gyros [12], or even four gyros [13], have been proposed to operate in a time division manner. A continuous mode reversal scheme has also been demonstrated [14], [15], but it did not reveal any results of improved bias instability [16]. Obviously, these methods indirectly avoid the hazards caused by the dead zone time of mode reversal gyro, but there is no improvement from the intrinsic mechanism of CVG. As a result, increasing mode switching speeds to solve dead zone problems is a critical and pressing task.

To the best of our knowledge, the topic of fast switching has not yet been paid enough attention to. Nevertheless, some indirect approaches are available since the switching process can be divided into ring up and ring down processes. As for the ring up function, the previous works resorted to analog demodulation and very high voltage driven solutions for gyro fast start-up, which not only come with a side effect of additional measurement noise, but also may increase the design complexity [17]–[19]. From the arithmetic aspect, most ring up and down functions only employ PI or linear output feedback controllers [8], [20], whereas advanced control methodologies have not been fully investigated for these applications.

Considering that mode reversal principle demands the ring up and down functions in a periodical pattern, the drive mode and the sense mode of the CVGs are required to be repeated alternately. It can therefore be formulated into a repetitive trajectory control problem [21]. Furthermore, the mode reversal as a discontinuous batch process has the characteristics of same initial states, and there is a certain time interval between two consecutive switchings. As a two-degree-of-freedom highly coupled

Manuscript received 29 June 2021; revised 17 April 2022 and 17 June 2022; accepted 14 July 2022. Recommended by Technical Editor D. Oetomo and Senior Editor Q. Zou. This work was supported in part by the National Natural Science Foundation of China under Grant 62171420 and in part by the Natural Science Foundation of Shandong Province under Grant ZR2020QF058. *(Corresponding author: Chong Li.)*

Yuchen Wang, Jiakun Hou, and Chong Li are with the Department of Automation and Measurement, Ocean University of China, Qingdao 266000, China (e-mail: wyc@stu.ouc.edu.cn; houjiakun@stu.ouc.edu.cn; lichong7332@ouc.edu.cn).

Jin Wu and Ming Liu are with the Department of Electronic and Computer Engineering, Hong Kong University of Science and Technology, Kowloon, Hong Kong (e-mail: jin_wu_uestc@hotmail.com; eelium@ust.hk).

Yu Jiang is with the ClearMotion, Inc., Billerica, MA 01821 USA (e-mail: yu.jiang@nyu.edu).

John Y. Hung is with the Department of Electrical and Computer Engineering, Auburn University, Auburn, AL 36849 USA (e-mail: hungjoh@auburn.edu).

Color versions of one or more figures in this article are available at https://doi.org/10.1109/TMECH.2022.3192393.

Digital Object Identifier 10.1109/TMECH.2022.3192393

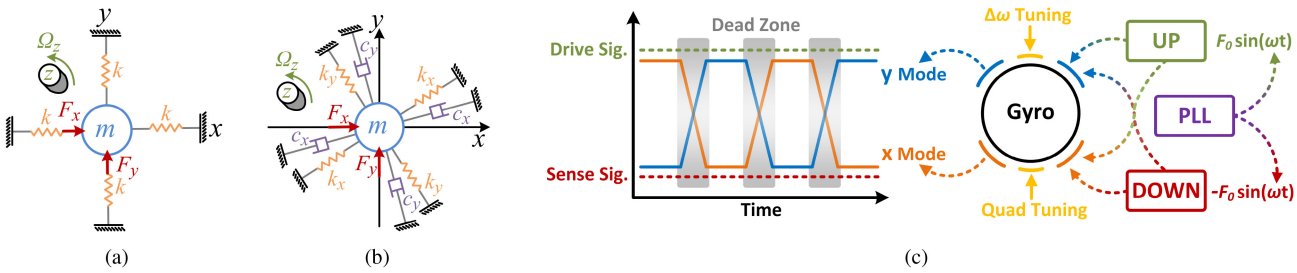

Fig. 1. Physical dynamics model of CVGs are equivalent to a two-degree-of-freedom lumped parameter system in Cartesian coordinates. (a) Ideal conditions. (b) Nonideal conditions. (c) Working principle of the mode reversal scheme.

resonator system, the internal mechanism of gyro is relatively complex to be obtained accurately. Therefore, iterative learning control (ILC) is a powerful approach [22]. This work analyzes the inherent characteristics of mode reversal and proposes an ultrafast switching control solution based on ILC. The contributions of this article are summarized as follows:

1) The physical model of CVG mode reversal task is formulated to show the issue of dead zone caused by slow switching speed. The theoretical and experimental analysis demonstrate that nonlinearity, cross coupling terms, and time-varying effects are preventing CVGs from a fast switching manner.
2) A novel iterative learning scheme for mode reversal gyroscopes is proposed to achieve ultra-fast switching function to reduce the dead zone problem. The ILC control law, that can adjust the causal and noncausal control effect, is shown to be robust to nonlinearity, cross coupling and time-varying. Based on this, the iterative learning controllers of the two gyro modes are designed to deal with the challenge of fatal problems.
3) The effectiveness and reliability of the proposed scheme are implemented and experimentally verified with an MEMS gyro. The switching time can reach a state-of-the-art level that less than 200 ms and is well maintained during the long-term evaluation to prove its robustness.

The remainder of this article presents the details.

II. Working Principle for Mode Reversal

A. Dynamics Modeling

Generally, CVGs are equivalent to physical models of resonators for analysis as shown in Fig. 1(a). By applying an alternating electrostatic force to the x mode, the resonator vibrates continuously around the resonant frequency of the x mode. In this case, the signal output by the x mode is regarded as the drive signal. This actuation process, also known as gyro start up, is defined as the ring up function. At this time, the Coriolis inertial force forms an alternating couple of forces acting on the y mode. The vibration amplitude of the y mode is proportional to the Coriolis inertial force. This sense signal from y mode is proportional to the angular velocity of the carrier in the vertical direction.

The above case is one of the two mode reversal working frames, i.e., x is the drive mode and y is the sense mode. Likewise, the second working frame of mode reversal is the opposite, i.e., x is the sense mode and y is the drive mode. The dynamics of the CVGs for both two modes are constructed as illustrated in Fig. 1(b), that can be written as

$$\begin{aligned} \ddot{x} + d_x\dot{x} + k_x x + d_{yx}\dot{y} + k_{yx}y &= F_x - 2\lambda\Omega_z\dot{y} \\ \ddot{y} + d_y\dot{y} + k_y y + d_{xy}\dot{x} + k_{xy}x &= F_y + 2\lambda\Omega_z\dot{x} \end{aligned} \tag{1}$$

where x and y are the displacement of the gyro mass in the two directions. Components of d_x and d_y denote the damper coefficients of the two vibrating modes. Terms of k_x and k_y are the spring coefficients of the two modes. The resonant frequencies related to spring coefficients of the two modes are defined as $\omega_x = \sqrt{k_x/m}$ and $\omega_y = \sqrt{k_y/m}$. For the coupling terms, k_{xy} and k_{yx} are the stiffness coupling coefficients between each vibrating modes, d_{xy} and d_{yx} are the damper coupling coefficients. Terms of $2m\Omega_z\dot{y}$ and $2m\Omega_z\dot{x}$ are the Coriolis effect induced components. F_x and F_y are defined as the alternating electrostatic drive force that can be written as

$$\begin{aligned} F_x &= \frac{S\varepsilon_0\varepsilon_r V_x^2}{2m(x-x_0)^2} \\ F_y &= \frac{S\varepsilon_0\varepsilon_r V_y^2}{2m(y-y_0)^2} \end{aligned} \tag{2}$$

where S is the area of the capacitor plate, m represents the effective mass of the mass, ε_0 and ε_r represent the vacuum permittivity coefficient and the permittivity dielectric coefficient, respectively. Components of x_0 and y_0 denote the initial capacitance channel width. Components of V_x and V_y are the electrostatic voltages of the two modes. The ring up and down functions of the x mode are time-multiplexed on V_x. The same is true for the y mode.

B. Principle of Mode Reversal

The alternating switching of the first and second working frames is the basic working principle of the advanced mode reversal gyro technology. As shown in Fig. 1(c), the mode reversal gyro uses a phase-locked loop (PLL) to generate the resonant frequencies for the ring up and ring down function. In the first working frame, the ring up function transmits an electrostatic force to the x mode to drive the gyroscopic vibration, and the ring down function transmits an electrostatic force to the y mode for suppressing operation. In this case, the x mode outputs

the drive detection signal, and the y mode outputs the sense detection signal. When the mode switch starts, the gyro system enters the dead zone state, and the angular rate signal cannot be sensed at this time. The end of the switch means the end of the dead zone, and the system then enters the second working frame, which is completely opposite to the first frame. During the whole process, the electrostatic tuning technology uses the spring softening effect to adjust the stiffness mismatch (k_x and k_y) induced frequency split and stiffness coupling (k_{xy} and k_{yx}) induced quadrature errors.

When gyro works in the first frame, y is much smaller than x, so it is assumed that the Coriolis force term of the x mode $2\lambda\Omega_z\dot{y}$ is zero. The Laplace transform method is utilized to solve the dynamic model [6]. By implementing an I/Q demodulation, the extracted in-phase signal including angular rate information still contains the in-phase error, which is the so-called bias error expressed in the time-domain expression of the y mode as follows:

$$y(t) = \frac{Q_x F_0}{m\omega_x^2} \frac{(2\lambda\Omega_z + \rho_{xy}) \sin(\omega_x t)}{\sqrt{(2\Delta\omega)^2 + (\omega_y/Q_y)^2}} \tag{3}$$

where the mode split is defined as the difference between two resonance frequencies, i.e., $\Delta\omega = \omega_x - \omega_y$. After the gyro is reversed once, the gyro system enters the second working frame. The time-domain expression of the x mode can be written as

$$x(t) = \frac{Q_y F_0}{m\omega_y^2} \frac{(-2\lambda\Omega_z + \rho_{yx}) \sin(\omega_y t)}{\sqrt{(2\Delta\omega)^2 + (\omega_x/Q_x)^2}}. \tag{4}$$

Under the condition of mode matching, i.e., $\Delta\omega = \omega_x - \omega_y = 0$, by detecting the signals on the two axes and making the difference, we can get

$$y(t) - x(t) = \frac{Q_x Q_y F_0}{m\omega^3} (4\lambda\Omega_z) \sin(\omega t) \tag{5}$$

which indicates the bias error source cancellation and doubles the scale factor. However, the results in (5) are obtained with time-sharing driving. Although mode reversal has such excellent advantages, its dead zone issue described in Fig. 1(c) still limits its development. Obviously, improving the transient performance of the ring up and ring down function to reduce the dead time can significantly improve the dynamic characteristics of the mode reversal gyroscope, which is an urgent problem to be solved.

III. Mode Reversal System Characterization

A. Major Challenges to Fast Reversal

As a high-end system, there are serious issues to achieve an ultrahigh-speed mode reversal gyro.

1) Nonlinearity: When the applied alternating electrostatic force continues to increase, the response of the gyro is not linear. The reason is due to the nonlinearity of electrostatic force that is described in (2). This problem results in a limited performance of the ring up and ring down function during switching transients, which exacerbates the dead zone issue.

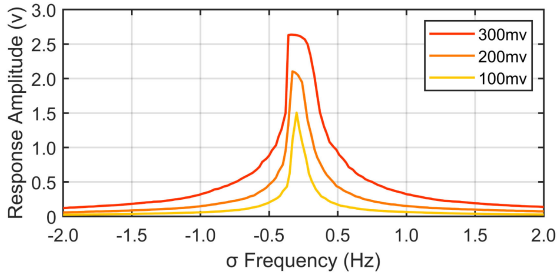

Fig. 2. Amplitude-frequency characteristic curve of the CVG by frequency sweeping technology. When the alternating excitation force amplitude is set to 100 mv, the response curve is basically in the linear region. When the amplitude increases to 300 mv, the gyro exhibits strong nonlinearity.

2) Mode Coupling: The electrostatic tuning technology can guarantee the steady-state coupling error suppression effect. Under the condition of mode reversal, however, terms of x and y are constantly changing. As a result, the coupling situation between them also changes accordingly, which makes the effect of tuning technology impaired. This leads to the problem of uncertain mode cross coupling during switching transients.

3) Time-Varying: In our previous work [5], [8], we analyzed the environment-induced time-varying characteristics of the CVGs, which is due to thermal effects caused by molecular thermal motion in the Coriolis gyroscope. For the control algorithm, the tracking effect may be different at different times during the long-term operation, which undoubtedly challenges the traditional feedback control algorithm.

B. Hardware Configuration

To evaluate the above-mentioned problems, we developed high-speed interface circuits for MEMS gyroscopes to realize the measurement and control system. The field programmable gate array (FPGA) can achieve high-speed I/Q demodulation to obtain in-phase and quadrature-phase baseband signals. The ARM core interconnected with the FPGA is designed to process the control algorithm at the baseband level.

C. Model Characteristics of the Plant

We experimentally verified the theoretical analysis from the three aspects with MEMS gyros in the same batch, pointing out the characteristics and difficulties of the plants.

1) Strong Nonlinearity: In order to verify the nonlinearity, we used a gyro to implement a frequency sweeping experiment, the result is shown in Fig. 2. Due to the drift of the resonance point, the normalized σ frequency is used to represent the results.

The results show that as the electrostatic driving force continues to increase, the response amplitude does not increase linearly. Meanwhile, the shape of the resonance peak changes obviously owing to what is described in (2). This is due to the nonlinear relationship between the voltage signal output by the ring up function and the electrostatic force signal actually received by the gyro.

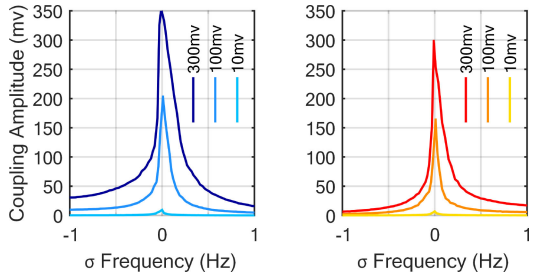

Fig. 3. Frequency sweeping results with quadrature tuning turned ON. When the driving force of the x mode is set to 10, 100, and 300 mv (left), the y mode (blue) is detected with varying degrees of coupling amplitude; when driving the y mode (right), the x mode (orange) also has a coupled signal.

2) Mode Coupling: To evaluate such issues of CVGs, we conducted a series of frequency sweeping experiments as shown in Fig. 3. The sweep technique can be regarded as an open-loop ring up function for multiple frequency points.

After implementing electrostatic tuning, the coupling problem in the case of a 10 mv drive signal is significantly improved. However, as the driving signal continues to increase, the effect of tuning technology is no longer obvious, causing the coupling problem to become more serious. Specifically, terms of k_{xy}, k_{yx}, d_{xy}, d_{yx} form destructive disturbances in a cross-coupled manner during transients. At the moment of switching, the intensity of the electrostatic force is highly amplified due to the rapid response of the ring up function. That is, mode reversal gyroscopes suffer from repeatable cross coupling at each switching dead zone.

3) Time-Varying Characteristics: In order to intuitively reflect the long-term changes, the data of the controller are collected with the mode reversal. From the start of power on for 10 min, the frequencies are collected every 30 min, and the average values of steady-state data of each period are shown in Fig. 4(a). Similarly, the steady-state average results of ring up and ring down functions are illustrated in Fig. 4(b).

As shown in Fig. 4(a), the change in k_x and k_y causes the frequencies to drift in a small range. The 10× error bar shows that the frequency difference is only a small change of about 0.2 Hz. This indicates that the frequencies do not have large transients during the switching dead zone. Fig. 4(b) presents the steady-state amplitude time-varying problem. This is due to the thermal drift of d_x and d_y. It can be seen that the dynamics of the gyro after entering the steady state are relatively insignificant.

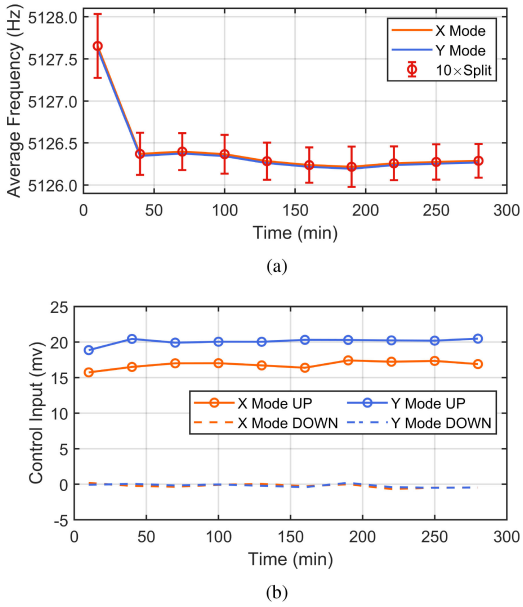

Fig. 4. Gyro system exhibits strong time-varying characteristics under long-term mode reversal operation. (a) Resonant frequency changes of the x mode (orange) and the y mode (blue) are basically the same. (b) After entering the steady state, the control inputs of the x mode (orange) and the y mode (blue) fluctuate within a certain range.

IV. Iterative Learning System Design

A. Novel Iterative Learning Law

Herein, we adopt the idea of iterative learning to solve the three key problems of the mode reversal gyro, and thus introduce the concept of iteration domain. Compared to feedback control in the time domain, ILC learns previous control information to form a feedforward signal for this iteration. Thus it achieves the capability of model-less control by accomplishing closed-loop feedback in the iteration domain.

In order to solve the nonlinearity and coupling problems of the reversal dead zone, in addition to causal control, noncausal control must be introduced to compensate for repetitive switching disturbances in advance. The proportional-differential (PD)-type ILC has the ability to meet the above two control needs. However, the differential term suffers from measurement noise, making its performance limited in practical applications.

To this end, this article proposes a novel sampled-data current-future (CF)-type ILC control law based on previous iteration errors. The approach can achieve noncausal control while avoiding the use of differentiation of errors. Robustness to time-varying problems is also a feature of this method. Importantly, the dimension of the learning step can be adjusted through the sample period Δt, which is suitable for the algorithm implementation in the actual noncausal control processor. The novel ILC law for gyro mode reversal is proposed as

$$\begin{aligned}\boldsymbol{u}_k(n\Delta t) = \boldsymbol{u}_{k-1}(n\Delta t) \\ + K_f \boldsymbol{e}_{k-1}((n+1)\Delta t) + K_c \boldsymbol{e}_{k-1}(n\Delta t)\end{aligned} \quad (6)$$

where Δt denotes the sampling period that satisfies $n\Delta t \leq t < (n+1)\Delta t$, $n = 0, 1, 2, \ldots, N$ and N is the gyro baseband signal sampling point with $N\Delta t = T$, where T is the gyro mode reversal period; $k = 0, 1, 2, \ldots, \mathcal{K}$ denote the iteration number; K_f and K_c are the learning parameters; $\boldsymbol{u}_k$ and $\boldsymbol{e}$ are the control input and error, which are defined in detail later. In the following analysis, $n\Delta t$ is abbreviated as n for convenience.

B. Convergence Analysis

Theorem 1: If the proposed control law (6) that applied in a CVG satisfies the following conditions.

(C1) The learning parameter K_f is properly tuned such that

$$\sup_k \max_{n\in\{0,1,\ldots,N\}} \left\| \boldsymbol{I} - K_f \boldsymbol{C} \int_n^{n+1} f_u\left(\boldsymbol{x}_k(\tau), \boldsymbol{\psi}_k(\tau)\right) d\tau \right\| \leq \rho < 1 \tag{7}$$

where $\boldsymbol{\psi}_k(t) \in [\boldsymbol{u}_k(t), \boldsymbol{u}_{d,k}(t)]$ and $0 < \rho < 1$. Other symbols are defined later.

(C2) The sampling period Δt, the learning parameter K_c and the mode reversal period T is small enough.

Then one can guarantee that the tracking error $\boldsymbol{e}_k(n)$ of the iterative learning mode reversal gyro converges to a bound.

Remark 1: The concept of being small enough is relative. The learning sampling period Δt is small enough relative to the gyro switching settling time t_{st}, which needs to be adjusted to the millisecond level. The mode reversal period T is small enough with respect to the time-varying of the gyro parameters, which is recommended on the order of seconds. The tuning guideline presents the details.

Proof: During one vibration period, the slowly varying parameters relative to the high frequency oscillatory signal are considered to be constant [23]. Perturbation methods are often utilized to reduce the order of the CVG model to obtain a first-order system at the baseband signal level. Therefore, consider a nonlinear order-reduced CVG system from (1) as

$$\begin{cases} \dot{\boldsymbol{x}}_k(t) = f\left(\boldsymbol{x}_k(t), \boldsymbol{u}_k(t)\right) + \boldsymbol{w}_{k,d}(t) + \boldsymbol{w}_{k,r}(t) \\ \boldsymbol{y}_k(t) = \boldsymbol{C}\boldsymbol{x}_k(t) + \boldsymbol{v}_k(t) \end{cases} \tag{8}$$

where $\boldsymbol{y}_k(t) \in \mathbb{R}^4$, $\boldsymbol{u}_k(t) \in \mathbb{R}^4$ and $\boldsymbol{x}_k(t) \in \mathbb{R}^4$ are the baseband output, baseband input and state of the reduced-order two gyro modes with in-phase and quadrature-phase, respectively; $t \in [0, T]$; $\boldsymbol{w}_{k,d}(t) \in \mathbb{R}^4$ is non-repetitive disturbance, and $\boldsymbol{w}_{k,r}(t) \in \mathbb{R}^4$ is repetitive interference caused by gyro cross-coupling; $\boldsymbol{v}_k(t) \in \mathbb{R}^4$ denotes the mechanical and circuit measurement noise bounded to β_v; $\boldsymbol{C} \in \mathbb{R}^{4\times4}$ is the gyro output transduction gain; $f(\cdot) : \mathbb{R}^8 \to \mathbb{R}^4$ is an unknown gyro nonlinear function, which contains electrostatic drive nonlinearities. Terms of $f_x(\cdot)$ and $f_u(\cdot)$ are defined as the partial derivatives with state and control input, respectively.

Remark 2: The time t is defined within the interval of the mode reversal period T. The latter is suggested to be tuned to be small enough, which is needed to solve the time-varying problem. This is to allow the ILC to track the time-varying gyro parameters in $f(\cdot)$, which does not require an accurate model and identification of $f(\cdot)$.

Remark 3: Disturbances are classified as nonrepetitive $\boldsymbol{w}_{k,d}(t)$ and repetitive $\boldsymbol{w}_{k,r}(t)$ according to the control task of repetitive mode reversal. The former corresponds to external unexpected disturbances, and the latter is caused by gyro cross-coupling. If these two are reasonable and bounded, the subsequent process proves that the control law in (6) is robust to it.

Remark 4: The perturbation method averages the gyro dynamics in (1), reducing it to a first-order nonlinear model in (8). The theoretical premise of this process is that the in-phase and quadrature-phase of the high-frequency vibration signal x and y relative to the baseband signal $\boldsymbol{y}_k(t)$ is usually many orders of magnitude higher, so $\boldsymbol{y}_k(t)$ can be considered constant within a vibration period.

The control objective is to let the error $\boldsymbol{e}_k(t) \triangleq \boldsymbol{y}_{d,k}(t) - \boldsymbol{y}_k(t)$ converge with the continuous iteration, thereby optimizing the key problem of the mode reversal gyroscope. Herein, the λ-norm of $\Pi(n)$ is defined as $\|\Pi(n)\|_\lambda = \max_{n\in\{0,\ldots,N\}} e^{-\lambda n}\|\Pi(n)\|$, where λ denotes a positive constant large enough.

Define a desired control input $\boldsymbol{u}_{d,k}(t)$ that can generate the desired output trajectory $\boldsymbol{y}_{d,k}(t)$ as

$$\begin{cases} \dot{\boldsymbol{x}}_{d,k}(t) = f\left(\boldsymbol{x}_{d,k}(t), \boldsymbol{u}_{d,k}(t)\right) \\ \boldsymbol{y}_{d,k}(t) = \boldsymbol{C}\boldsymbol{x}_{d,k}(t) \end{cases}. \tag{9}$$

Although the gyro parameters are time-varying, they are always bounded within a reasonable range. The key effect of the time-varying problem on ILC is to change the initial error. The initial errors and the iteration control input varying are bounded, i.e., $\sup_k \|\boldsymbol{x}_{d,k}(0) - \boldsymbol{x}_k(0)\| \leq \beta_{\delta x_0}$, $\sup_k \max_{t\in[0,T]} \|\Delta\boldsymbol{u}_{d,k}(t)\| \leq \beta_{\Delta u_d}$ where $\triangle\boldsymbol{u}_{d,k}(t) \triangleq \boldsymbol{u}_{d,k}(t) - \boldsymbol{u}_{d,k-1}(t)$. Assuming that the CVG system is locally Lipschitz continuous, that is

$$\|f\left(\mathscr{G}_{d,k}(t)\right) - f\left(\mathscr{G}_k(t)\right)\| \leq L(Z_k(t))\,\|\mathscr{G}_{d,k}(t) - \mathscr{G}_k(t)\| \tag{10}$$

where $\mathscr{G}_k(t) \triangleq [\boldsymbol{x}_k(t),\ \boldsymbol{u}_k(t)], \mathscr{G}_{d,k}(t) \triangleq [\boldsymbol{x}_{d,k}(t), \boldsymbol{u}_{d,k}(t)]$, $L(Z_k(t))$ is a Lipschitz-like function depending on $Z_k(t) = \theta\mathscr{G}_{d,k}(t) + (1-\theta)\mathscr{G}_k(t)$, $\theta \in [0,1]$; $L(Z_k(t))$ follows:

$$L(Z_k(t)) \leq \phi(t)\alpha(\|Z_k(t)\|) + \sigma(t) \tag{11}$$

where $\alpha(\cdot) : [0,\infty) \to [0,\infty)$ is an unknown strictly increasing function; $\phi(t) \in [0, b_\phi]$ and $\sigma(t) \in [0, b_\sigma]$ are finite with each mode reversal period; $Z_k(t)$ is bounded to $\bar{\beta}_Z$ such that [24]

$$\begin{aligned} &\max_{k\in\{0,\ldots,\mathcal{K}\}} \max_{t\in[0,T]} |L\left(Z_k(t)\right)| \\ &\leq \max_{k\in\{0,\ldots,\mathcal{K}\}} \max_{t\in[0,T]} \left[\phi(t)\alpha\left(\|Z_k(t)\|\right) + \sigma(t)\right] \\ &\leq b_\phi\alpha\left(\bar{\beta}_Z\right) + b_\sigma \triangleq \bar{\beta}_L. \end{aligned} \tag{12}$$

According to the differential mean value theorem (10) and (12), one can obtain

$$\begin{aligned} &\|f\left(\boldsymbol{x}_{d,k}(t), \boldsymbol{u}_{d,k}(t)\right) - f\left(\boldsymbol{x}_k(t), \boldsymbol{u}_k(t)\right)\| \\ &= \|f_x\left(\boldsymbol{\xi}_k(t), \boldsymbol{u}_{d,k}(t)\right)\delta\boldsymbol{x}_k(t) + f_u\left(\boldsymbol{x}_k(t), \boldsymbol{\psi}_k(t)\right)\delta\boldsymbol{u}_k(t)\| \\ &= \left\|\left[f_x\left(\boldsymbol{\xi}_k(t), \boldsymbol{u}_{d,k}(t)\right), f_u\left(\boldsymbol{x}_k(t), \boldsymbol{\psi}_k(t)\right)\right]\left(\mathscr{G}_{d,k}(t) - \mathscr{G}_k(t)\right)^\top\right\| \\ &\leq \|[f_x\left(\boldsymbol{\xi}_k(t), \boldsymbol{u}_{d,k}(t)\right), f_u\left(\boldsymbol{x}_k(t), \boldsymbol{\psi}_k(t)\right)]\|\,\|\mathscr{G}_{d,k}(t) - \mathscr{G}_k(t)\| \\ &\leq \bar{\beta}_L\,\|\mathscr{G}_{d,k}(t) - \mathscr{G}_k(t)\| \end{aligned} \tag{13}$$

where $\delta\boldsymbol{u}_k(t) \triangleq \boldsymbol{u}_{d,k}(t) - \boldsymbol{u}_k(t)$, $\boldsymbol{\xi}_k(t) \in [\boldsymbol{x}_k(t), \boldsymbol{x}_{d,k}(t)]$, $\boldsymbol{\psi}_k(t) \in [\boldsymbol{u}_k(t), \boldsymbol{u}_{d,k}(t)]$. That is

$$\begin{aligned} \max_{k\in\{0,\ldots,\mathcal{K}\}} \max_{t\in[0,T]} \|f_x\left(\boldsymbol{\xi}_k(t), \boldsymbol{u}_{d,k}(t)\right)\| &\leq \bar{\beta}_L \\ \max_{k\in\{0,\ldots,\mathcal{K}\}} \max_{t\in[0,T]} \|f_u\left(\boldsymbol{x}_k(t), \boldsymbol{\psi}_k(t)\right)\| &\leq \bar{\beta}_L. \end{aligned} \tag{14}$$

The state error $\delta\boldsymbol{x}_k(t) \triangleq \boldsymbol{x}_{d,k}(t) - \boldsymbol{x}_k(t)$. Thereafter, since the gyro processor system updates once every Δt, i.e., $\boldsymbol{u}_k(t) = \boldsymbol{u}_k(n)$ for $t \in [n\Delta t, (n+1)\Delta t)$, one has

$$\begin{aligned}\|\delta\boldsymbol{u}_k(t)\| &= \|\boldsymbol{u}_{d,k}(t) - \boldsymbol{u}_{d,k}(n) + \boldsymbol{u}_{d,k}(n) - \boldsymbol{u}_k(t)\| \\ &= \|\boldsymbol{u}_{d,k}(t) - \boldsymbol{u}_{d,k}(n) + \boldsymbol{u}_{d,k}(n) - \boldsymbol{u}_k(n)\| \\ &\le \beta_{\tilde{u}} + \|\delta\boldsymbol{u}_k(n)\| \end{aligned} \tag{15}$$

where $\beta_{\tilde{u}} = \sup_k \max_{n\in\{0,1,\ldots,N\}} \|\boldsymbol{u}_{d,k}(t) - \boldsymbol{u}_{d,k}(n)\|$. Since the time t is included between two samples of the gyro processing system, one has $\boldsymbol{x}_k(t) = \boldsymbol{x}_k(n) + \int_n^t \dot{\boldsymbol{x}}_k(\tau)d\tau$. Then from [25], one can obtain

$$\begin{aligned}\|\delta\boldsymbol{x}_k(t)\| \le \bar{\Xi}_1 \|\delta\boldsymbol{x}_k(n)\| + \bar{\Gamma}(\Delta t)\|\delta\boldsymbol{u}_k(n)\| \\ + \bar{\Gamma}(\Delta t)\left(\beta_{\tilde{u}} + \beta_w/\bar{\beta}_L\right)\end{aligned} \tag{16}$$

where $\bar{\Xi}_1 = e^{\bar{\beta}_L \Delta t} > 1$, $\bar{\Gamma}(\Delta t) = e^{\bar{\beta}_L\Delta t}\bar{\beta}_L\Delta t$, and

$$\begin{aligned}\|\delta\boldsymbol{x}_k(n)\| \le \bar{\Xi}_1^N \beta_{\delta x_0} + \bar{\Gamma}(\Delta t)\sum_{j-0}^{n-1}\bar{\Xi}_1^{n-1-j}\|\delta\boldsymbol{u}_k(j)\| \\ + \frac{\bar{\Xi}_1^N - 1}{\bar{\Xi}_1 - 1}\bar{\Gamma}(\Delta t)\left(\beta_{\tilde{u}} + \beta_w/\bar{\beta}_L\right)\end{aligned} \tag{17}$$

where β_w is the bound of generalized disturbance $\boldsymbol{w}_k(t)$ acting on order-reduced CVG dynamics, which can be considered as $\boldsymbol{w}_k(t) = \boldsymbol{w}_{k,n}(t) + \boldsymbol{w}_{k,r}(t)$.

According to (8) and (9), one has

$$\begin{aligned}&K_f\boldsymbol{e}_k(n+1) + K_c\boldsymbol{e}_k(n) \\ &= K_f\boldsymbol{C}\left(\boldsymbol{x}_{d,k}(n) - \boldsymbol{x}_k(n)\right) - K_f\boldsymbol{v}_k(n+1) \\ &\quad + K_c\boldsymbol{C}\left(\boldsymbol{x}_{d,k}(n) - \boldsymbol{x}_k(n)\right) - K_c\boldsymbol{v}_k(n) \\ &\quad + K_f\boldsymbol{C}\int_n^{n+1}\left(\dot{\boldsymbol{x}}_{d,k}(\tau) - \dot{\boldsymbol{x}}_k(\tau)\right)d\tau \\ &= K_f\boldsymbol{C}\int_n^{n+1} f_u\left(\boldsymbol{x}_k(\tau), \boldsymbol{\psi}_k(\tau)\right)\delta\boldsymbol{u}_k(\tau)d\tau + \mathcal{B}_k(n)\end{aligned} \tag{18}$$

where

$$\begin{aligned}\mathcal{B}_k(n) = K_f\boldsymbol{C}\int_n^{n+1}\left(f_x(\boldsymbol{\xi}_k(\tau), \boldsymbol{u}_{d,k}(\tau))\delta\boldsymbol{x}_k(\tau) - \boldsymbol{w}_k(\tau)\right)d\tau \\ + K_f\boldsymbol{C}\delta\boldsymbol{x}_k(n) - K_f\boldsymbol{v}_k(n+1) \\ + K_c\boldsymbol{C}\delta\boldsymbol{x}_k(n) - K_c\boldsymbol{v}_k(n).\end{aligned} \tag{19}$$

Then we have

$$\begin{aligned}&\|\mathcal{B}_k(n)\| \\ &\le K_f\|\boldsymbol{C}\|\int_n^{n+1}\|f_x\left(\boldsymbol{\xi}_k(\tau), \boldsymbol{u}_{d,k}(\tau)\right)\|\,\|\delta\boldsymbol{x}_k(\tau)\|\,d\tau \\ &\quad + (K_f + K_c)\|\boldsymbol{C}\|\,\|\delta\boldsymbol{x}_k(n)\| + K_f\|\boldsymbol{C}\|\Delta t\beta_w + (K_f + K_c)\beta_v \\ &\le K_f\bar{\beta}_L\|\boldsymbol{C}\|\int_n^{n+1}\|\delta\boldsymbol{x}_k(\tau)\|\,d\tau + (K_f + K_c)\|\boldsymbol{C}\|\,\|\delta\boldsymbol{x}_k(n)\| \\ &\quad + K_f\|\boldsymbol{C}\|\Delta t\beta_w + (K_f + K_c)\beta_v.\end{aligned} \tag{20}$$

Substituting (16) into (20) yields

$$\begin{aligned}&\|\mathcal{B}_k(n)\| \\ &\le \bar{\beta}_L K_f\|\boldsymbol{C}\|\int_n^{n+1}\left(\bar{\Xi}_1\|\delta\boldsymbol{x}_k(n)\| + \bar{\Gamma}(\Delta t)\|\delta\boldsymbol{u}_k(n)\|\right. \\ &\quad \left. + \bar{\Gamma}(\Delta t)\left(\beta_{\tilde{u}} + \beta_w/\bar{\beta}_L\right)\right)d\tau \\ &\quad + (K_f + K_c)\|\boldsymbol{C}\|\,\|\delta\boldsymbol{x}_k(n)\| + K_f\|\boldsymbol{C}\|\Delta t\beta_w + (K_f + K_c)\beta_v \\ &= \left(K_f\bar{\beta}_L\bar{\Xi}_1\Delta t + K_f + K_c\right)\|\boldsymbol{C}\|\,\|\delta\boldsymbol{x}_k(n)\| \\ &\quad + K_f\bar{\beta}_L\bar{\Gamma}(\Delta t)\Delta t\|\boldsymbol{C}\|\,\|\delta\boldsymbol{u}_k(n)\| + K_f\|\boldsymbol{C}\|\Delta t\beta_w \\ &\quad + K_f\bar{\beta}_L\left(\beta_{\tilde{u}} + \beta_w/\bar{\beta}_L\right)\bar{\Gamma}(\Delta t)\Delta t\|\boldsymbol{C}\| + (K_f + K_c)\beta_v.\end{aligned} \tag{21}$$

According to (6), (15), and (18), one has

$$\begin{aligned}&\delta\boldsymbol{u}_{k+1}(n) = \delta\boldsymbol{u}_k(n) - K_f\boldsymbol{C} \\ &\quad \times\int_n^{n+1} f_u(\boldsymbol{x}_k(\tau), \boldsymbol{\psi}_k(\tau))(\boldsymbol{u}_{d,k}(\tau) - \boldsymbol{u}_{d,k}(n) + \delta\boldsymbol{u}_k(n))d\tau \\ &\quad - \mathcal{B}_k(n) + \Delta\boldsymbol{u}_{d,k+1}(n) \\ &= \left[\boldsymbol{I} - K_f\boldsymbol{C}\int_n^{n+1} f_u\left(\boldsymbol{x}_k(\tau), \boldsymbol{\psi}_k(\tau)\right)d\tau\right]\delta\boldsymbol{u}_k(n) \\ &\quad - K_f\boldsymbol{C}\int_n^{n+1} f_u\left(\boldsymbol{x}_k(\tau), \boldsymbol{\psi}_k(\tau)\right)\left(\boldsymbol{u}_{d,k}(\tau) - \boldsymbol{u}_{d,k}(n)\right)d\tau \\ &\quad - \mathcal{B}_k(n) + \triangle\boldsymbol{u}_{d,k+1}(n).\end{aligned} \tag{22}$$

Take the norm of (22) as

$$\begin{aligned}\|\delta\boldsymbol{u}_{k+1}(n)\| \le \left\|\boldsymbol{I} - K_f\boldsymbol{C}\int_n^{n+1} f_u\left(\boldsymbol{x}_k(\tau),\right.\right. \\ \left.\left.\boldsymbol{\psi}_k(\tau)\right)d\tau\right\|\,\|\delta\boldsymbol{u}_k(n)\| \\ + K_f\bar{\beta}_L\beta_{\tilde{u}}\Delta t\|\boldsymbol{C}\| + \|\mathcal{B}_k(n)\| + \beta_{\triangle u_d}.\end{aligned} \tag{23}$$

Substituting (17) and (21) into (23) yields

$$\begin{aligned}\|\delta\boldsymbol{u}_{k+1}(n)\| &\le \rho\|\delta\boldsymbol{u}_k(n)\| + K_f\bar{\beta}_L\beta_{\tilde{u}}\Delta t\|\boldsymbol{C}\| \\ &\quad + \left[K_f\bar{\beta}_L\bar{\Xi}_1\Delta t + K_f + K_c\right]\|\boldsymbol{C}\|\,\|\delta\boldsymbol{x}_k(n)\| \\ &\quad + K_f\bar{\beta}_L\bar{\Gamma}(\Delta t)\Delta t\|\boldsymbol{C}\|\,\|\delta\boldsymbol{u}_k(n)\| + K_f\|\boldsymbol{C}\|\Delta t\beta_w \\ &\quad + (K_f + K_c)\beta_v + K_f\bar{\beta}_L\left(\beta_{\tilde{u}} + \beta_w/\bar{\beta}_L\right) \\ &\quad \times\bar{\Gamma}(\Delta t)\Delta t\|\boldsymbol{C}\| + \beta_{\triangle u_d} \\ &\le \bar{\rho}_1\|\delta\boldsymbol{u}_k(n)\| + \bar{\Xi}_2\sum_{j=0}^{n-1}\bar{\Xi}_1^{n-1-j}\|\delta\boldsymbol{u}_k(j)\| + \bar{\Xi}_3\end{aligned} \tag{24}$$

where

$$\begin{aligned}
\bar{\rho}_1 &= \rho + K_f\bar{\beta}_L\|\boldsymbol{C}\|\bar{\Gamma}(\Delta t)\Delta t \\
\bar{\Xi}_2 &= \left[K_f\|\boldsymbol{C}\|\bar{\beta}_L\bar{\Xi}_1\Delta t + K_f\|\boldsymbol{C}\| + K_c\|\boldsymbol{C}\|\right]\bar{\Gamma}(\Delta t) \\
\bar{\Xi}_3 &= K_f\|\boldsymbol{C}\|\bar{\beta}_L\Delta t\left[\beta_{\tilde{u}} + \left(\beta_{\tilde{u}} + \beta_w/\bar{\beta}_L\right)\bar{\Gamma}(\Delta t)\right] \\
&\quad + \left[K_f\|\boldsymbol{C}\|\bar{\beta}_L\bar{\Xi}_1\Delta t + K_f\|\boldsymbol{C}\| + K_c\|\boldsymbol{C}\|\right] \\
&\quad \times \left[\left(\beta_{\tilde{u}} + \beta_w/\bar{\beta}_L\right)\bar{\Gamma}(\Delta t)\frac{\bar{\Xi}_1^N - 1}{\bar{\Xi}_1 - 1} + \Xi_1^N\beta_{\delta x_0}\right] \\
&\quad + K_f\|\boldsymbol{C}\|\Delta t\beta_w + (K_f + K_c)\beta_v + \beta_{\Delta u_d}. \qquad (25)
\end{aligned}$$

If Δt is small enough, since $\rho < 1$ according to condition C1, one has $\bar{\rho}_1 < 1$. Following the technical procedure in [24], one can obtain $\sup_k \max_{t\in[0,T]} \|Z_k(t)\| \le b_Z$, $\beta_L = b_\phi\alpha(b_Z) + b_\sigma$, $\Gamma(\Delta t) = e^{\beta_L\Delta t}\beta_L\Delta t$, and the iterative learning mode reversal convergence based on conditions C1 and C2 is as follows:

$$\begin{aligned}
\lim_{k\to\infty}\|\boldsymbol{e}_k(n)\|_\lambda &\le \|\boldsymbol{C}\|\Gamma(\Delta t)\frac{1 - \Xi_1^{-(\lambda-1)N}}{\Xi_1^\lambda - \Xi_1}\frac{\Xi_3}{1-\rho_2} + \beta_v \\
&\quad + \|\boldsymbol{C}\|\left[\Xi_1^N\beta_{\delta x_0} + \frac{\Xi_1^N - 1}{\Xi_1 - 1}\Gamma(\Delta t)\left(\beta_{\tilde{u}} + \beta_w/\beta_L\right)\right] \qquad (26)
\end{aligned}$$

where $0 < \rho_2 < 1$; $\Xi_1 = e^{\beta_L\Delta t}$; and

$$\begin{aligned}
\Xi_3 &= K_f\|\boldsymbol{C}\|\beta_L\Delta t\left[\beta_{\tilde{u}} + \left(\beta_{\tilde{u}} + \beta_w/\beta_L\right)\Gamma(\Delta t)\right] \\
&\quad + \left[K_f\|\boldsymbol{C}\|\beta_L\Xi_1\Delta t + K_f\|\boldsymbol{C}\| + K_c\|\boldsymbol{C}\|\right] \\
&\quad \times \left[\left(\beta_{\tilde{u}} + \beta_w/\beta_L\right)\Gamma(\Delta t)\frac{\Xi_1^N - 1}{\Xi_1 - 1} + \Xi_1^N\beta_{\delta x_0}\right] \\
&\quad + K_f\|\boldsymbol{C}\|\Delta t\beta_w + (K_f + K_c)\beta_v + \beta_{\Delta u_d}. \qquad (27)
\end{aligned}$$

An immediate result is that the convergence mainly depends on the learning parameters K_f and K_c, time interval Δt, initial state error $\beta_{\delta x_0}$, and disturbance and noise. □

C. Iterative Learning Mode Reversal

The proposed CF-type ILC control law is used to solve the dead zone problem of mode reversal. The principle is as follows:

1) Model Uncertainties Robustness: The time-domain open-loop control signal learned from repetitive mode reversal is highly robust to model uncertainties to fix the coupling and nonlinearity problems. Specifically, iterative learning compensates the repetitive coupling $\boldsymbol{w}_{k,r}(t)$ and nonlinearity $f(\cdot)$ in the CVG system (8) in advance through the closed loop in the iteration domain, so as to solve the lag problem of feedback control in transient tracking. By introducing the feedback of the future time and the current time of the previous error, i.e., $\boldsymbol{e}_{k-1}((n+1)\Delta t)$ and $\boldsymbol{e}_{k-1}(n\Delta t)$, a feedforward control instruction can be formed to complete the noncausal and causal control, respectively, thereby optimizing the repeated coupling and nonlinearity shown in Figs. 2 and 3. By fixing the problem of model-less switching dead zone, the reversal speed can be improved in principle.

2) Time-Varying Robustness: For the problems in Fig. 4(a), since the two frequencies are close, there is no large transient during the switching dead zone. A PI-based PLL feedback controller can be designed to meet the requirements. The problems illustrated in 4(b) can be solved by iterative learning, because the change of the gyro parameters is relatively slow. That is, even though the initial error $\|\boldsymbol{x}_{d,k}(0) - \boldsymbol{x}_k(0)\|$ varies in the iteration domain, it is still bound by $\beta_{\delta x_0}$ in the convergence with reasonable disturbances and noises. By designing the reversal period T that is sufficiently small relative to gyro time-varying, the ILC law can track parameters change in $f(\cdot)$ in time. In this way, the learned control input completes the closed-loop in the iteration domain, so as to compensate the time-varying error.

3) Parameter Tuning Guideline: Parameter adjustment needs to follow conditions C1 and C2 to ensure convergence and robustness. The tentative tuning guide is widely recommended in iterative learning [26]. Due to the conditions, low enough K_f and K_c are set and run for a sufficient number of iterations. After obtaining stable transient behavior and error performance, appropriate parameters are added to speed up the convergence, but too large parameters may quickly deteriorate transiently as implied in (7). Therefore, the tuning parameters need to be adjusted according to the actual learning results, and the gyro response must be closely monitored in the iterative process to ensure that it can eventually converge. As for the sampling period Δt, the proposed method has the ability to deal with the sampling period dimension problem of practical digital gyro processors, and different Δt and K_f in (6) jointly affect the learning effect of noncausal control. A rule of thumb, i.e., $0 < \Delta t \le 1/100\, t_{st}$ is recommended to satisfy C2, where t_{st} is the desired settling time. We choose Δt =1 ms for the tested MEMS mode reversal gyro. Besides, the reversal period T only needs to be set to the second level to track the time-varying parameters in time because the gyro parameters are slowly changing as shown in Fig. 4(b).

4) Learning Starting Points: In order to speed up the convergence process, the 0th iteration with traditional feedback control is adopted. Compared with directly using iterative learning for the 0th process, this scheme can equivalently reduce the initial error of the control input and state, i.e., $\beta_{\Delta u_d}$ and $\beta_{\delta x_0}$, thereby accelerating the convergence. This approach can be vividly understood as improving the starting points of iterative learning.

V. Experimental Validation

A. Preliminary Results of Iterative Learning Controller

We developed a prototype equipped with the proposed iterative learning scheme to perform mode reversal operations on the gyro. Following the turning procedure, the ring up and down learning processes are demonstrated as illustrated in Fig. 5(a) and (b), respectively. From the perspective of the iteration domain, the response and the control input of the first iteration are completed by PI, that is used to guide subsequent iterative learning. Until the 60th and 80th iterations, the settling time and stability have been substantially improved.

The signal $||\boldsymbol{e}_k||$ is small at the beginning, resulting from the PI used in the first iteration. In the subsequent learning process, the error slowly rises, and the response amplitude and control input fluctuate accordingly. After reaching the peak, the error has been declining continuously, achieving a better learning

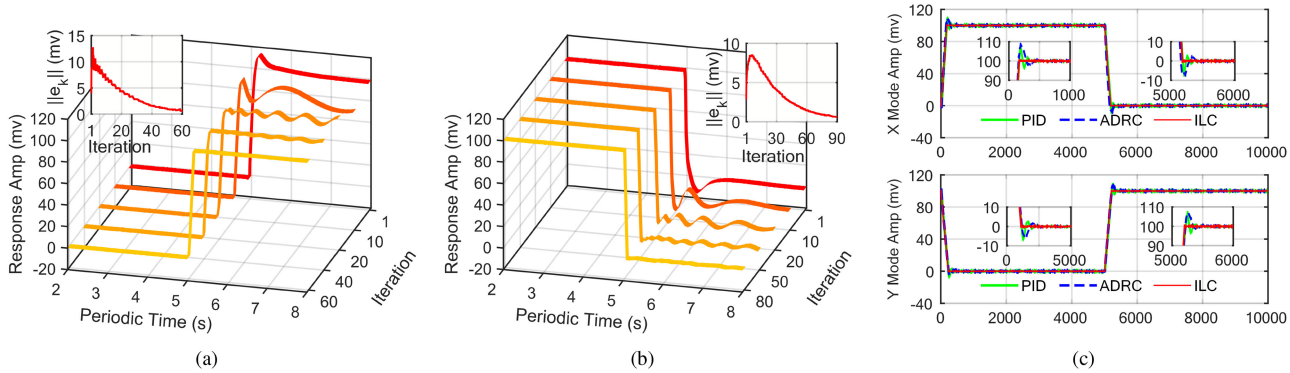

Fig. 5. (a) Iterative learning process results of the ring up function. (b) Iterative learning process results of the ring down function. (c) Fair comparison results of the three methods for the two modes.

effect. Compared with Fig. 5(b), the $||e_k||$ in Fig. 5(a) has larger chattering and amplitude, which may be due to the strong learning parameters, thereby shortening the convergence time of the learning process.

In the case of a 1.65 V polarization dc voltage with a set point of 100 mv, the settling time reaches the level of 150 ms, which is the state-of-the-art result [17]–[19], [27].

B. Comprehensive Evaluation Setup

In order to further verify the improvement and effectiveness of the proposed scheme, long-term operation tests with comparisons of other controllers were designed and performed. The long-term operation of the control algorithm should be evaluated because of the time-varying characteristics and environmental sensitivity. We conducted a 5-h mode reversal operation test on the three algorithms to simulate actual application scenarios. Ten minutes after the system power-ON, the gyro enters the working state, and the response amplitudes of the two modes were recorded. Thereafter, the data every 30 min were collected accordingly, and their settling time was determined from this.

The popular PID algorithm and the active disturbance rejection control (ADRC) algorithm are operated on the mode reversal gyro for comparison. The three control algorithms all face the problem of parameter tuning, which involves the tradeoff of the scheme. The parameter tuning procedures are given below to conduct a fair comparison.

1) As a classic controller, PID is common in gyro measurement and control systems [28]. We use the common Ziegler–Nichols method to tune the parameters of the control loops of the two vibration modes in the mode reversal gyro.

a) Set $K_P = 0$, $K_I = 0$ and $K_D = 0$, then increase K_P gradually until the response amplitude begins to oscillate. Record the current K_P as K_U and the oscillation period as T_U.

b) Let $K_P = 0.6K_U$, $K_I = 2K_P/T_U$ and $K_D = K_P T_U/8$ be the operation values of the PID controller.

2) ADRC is evolved from PID algorithm, which adopts the core concept of PID error feedback control. It has been proved to be an effective solution in system control and disturbance/uncertainty estimation [29], [30]. The ESO (extended state observer) has an extended state to track the combination of unknown parts of internal dynamics and unknown external disturbances, i.e., generalized disturbances d. It is composed of three outputs z_1, z_2, z_3 and three observer parameters β_1, β_2, β_3. Each can be expressed as

$$\begin{cases} \dot{z}_1 = z_2 + \beta_1 (y_k - z_1) \\ \dot{z}_2 = z_3 + \beta_2 (y_k - z_1) + Bu \\ \dot{z}_3 = \beta_3 (y_k - z_1). \end{cases} \tag{28}$$

When the parameters are well tuned, the three observer parameters track y_k, $\dot{y}_k$, and d, respectively. Terms of K_P, K_D, and B represent the controller parameters, and the control law is written as

$$\begin{aligned} u_0 &= K_P (y_{sp} - z_1) - K_D z_2 \\ u &= (u_0 - z_3)/B \end{aligned} \tag{29}$$

where y_{sp} is the set point of the response output. B needs to be selected to weigh the stability and response speed of the closed-loop system. We use the parameter tuning method proposed by Gao [29] to conduct experiments.

a) Get the desired settling time t_{st}.
b) Let $\omega_c = 10/t_{st}$, $K_P = \omega_c^2$ and $K_D = 2\omega_c$.
c) Let $\omega_o = 4\omega_c$, $\beta_1 = 3\omega_o$, $\beta_2 = 3\omega_o^2$ and $\beta_3 = \omega_o^3$.
d) Increase B gradually until the dynamic performance is satisfactory.

On the one hand, the aggressive electrostatic driving force brings strong transient growth performance, that is necessary for fast mode reversal gyro. On the other hand, excessive control input affects the instability of the control system and amplifies steady-state noise. We focus on the improvement of settling time without giving up the signal-to-noise ratio (SNR). Considering this, the steady-state performance of the three control algorithms is adjusted to be consistent to reflect the fairness of comparison, which is characterized by approximately equal noise swings of about 0.2 mv.

For a CVG system, excessive amplitude of the drive signal will undoubtedly cause the failure of the gyro excitation capacitor plate. According to the frequency sweeping results in

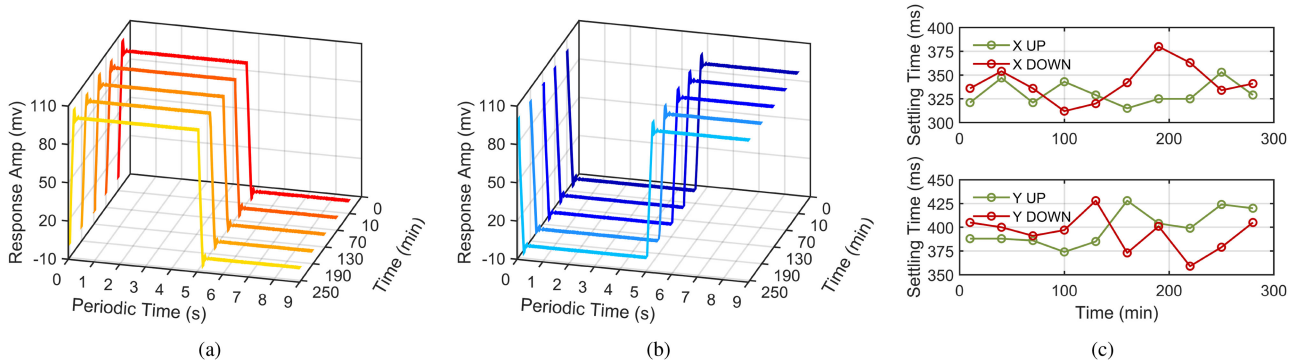

Fig. 6. Long-term test of the PID algorithm. (a) X mode results. (b) Y mode results. (c) Settling time change results.

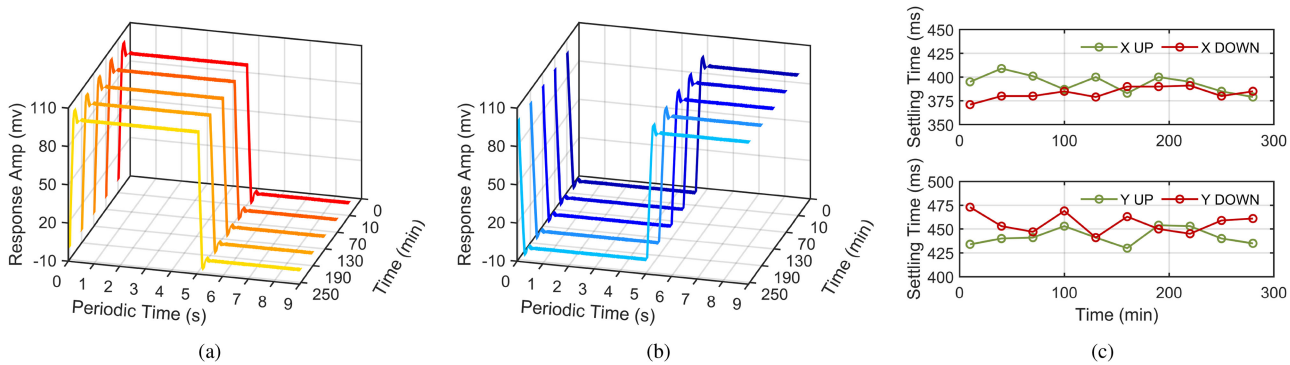

Fig. 7. Long-term test of the ADRC algorithm. (a) X mode results. (b) Y mode results. (c) Settling time change results.

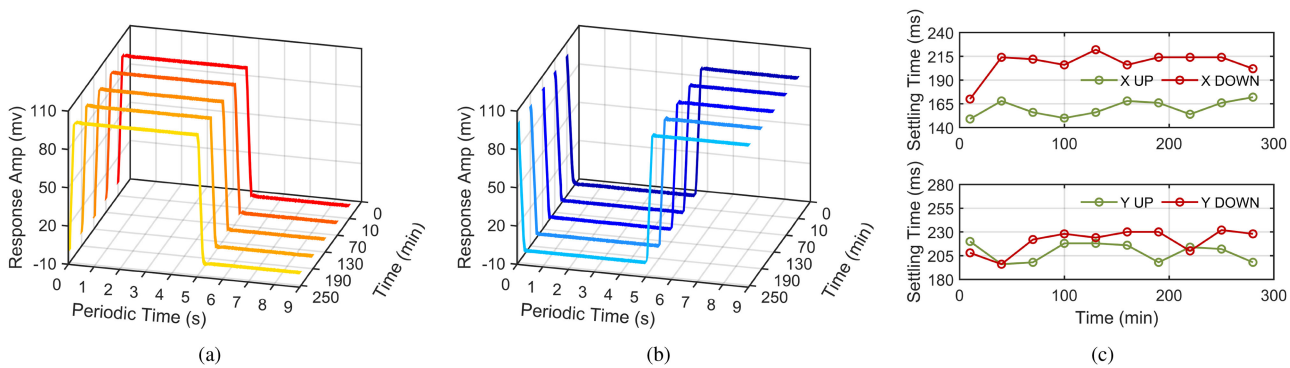

Fig. 8. Long-term test of the ILC algorithm. (a) X mode results. (b) Y mode results. (c) Settling time change results.

Fig. 2, the control input $\boldsymbol{u}$ of all three algorithms are limited to 300 and -250 mv for the ring up and ring down functions, respectively.

C. Comparative Analysis

The results of the three approaches after running for five hours are shown in Fig. 5(c). A noticeable feature is that ILC is superior to PID and ADRC in terms of settling time for both x mode and y mode. Hence, ILC is obviously more suitable for mode reversal gyros due to its rapidity. In detail, the response amplitudes for every hour and the settling time for every 30 min of the three algorithms are recorded in Figs. 6–8.

1) Parameter Tuning Complexity: ILC takes the longest time to tune the parameters because it needs a learning process, while the PID tuning is the simplest.

Each control method faces the steps of parameter tuning, and the overly complicated process will inevitably limit the promotion of the algorithm in practical applications. It is undeniable that the ILC tuning process is the longest, because each set of parameters requires a certain amount of learning time, especially conservative strategies. In contrast, the ADRC parameter tuning method is relatively easy, only needs to adjust the control input

parameter, observer bandwidth and controller bandwidth. For complex scenes, it may be necessary to adjust the observer gain and PD controller gain separately. PID tuning is relatively simplest and straightforward, which is one of the reasons for its popularity.

Although ILC has a complicated parameter tuning process, its learning data are collected by the memory and can be retrieved the next time it is used. In addition, the learning process of ILC can be turned ON or OFF in real time depending on the $||e_k||$. That is, it can realize online learning according to factors such as the slow change of the environment-induced error. The controller parameters of the other two methods are kept constant during long-term operation, and cannot be optimized accordingly with time-varying factors. Theoretically, they cannot deal with the change of the time-varying terms in the gyro.

2) Overshoot: The ILC overshoot is the smallest implying the best transient growth.

All three algorithms can provide decent transient overshoot due to relatively aggressive parameter tuning schemes. PID and ADRC quickly enter a steady state after experiencing a certain overshoot, but ILC has no obvious overshoot in the results of several hours, and the steady-state noise of the three algorithms meets the tuning expectations at the 0.2 mv level.

According to Fig. 6(a) and (b), the results show that the PID overshoot varies between 6 and 9%, indicating poor stability. The response amplitude of the ADRC also appears obvious overshoot as illustrated in Fig. 7(a) and (b). Fortunately, its over amplitude is controlled at around 7 to 8% that is directly related to the robustness provided by ESO. The overshoot of the ILC is usually kept within 1%, and occasionally exceeds 2%, demonstrating a good transient performance.

3) Settling Time: ILC demonstrates the shortest settling time and therefore best fits the goal of fast mode reversal.

As the core indicator of mode switching, the settling time needs to be comprehensively investigated. The results are recorded at 30-min intervals that are shown in Figs. 6(c), 7(c), and 8(c). In 5 h, their settling time fluctuated within a certain reasonable range. The results of PID are slightly better than that of ADRC, which may be caused by poor tuning parameters. Moreover, it also illustrates the complexity of ADRC tuning. For the stability of long-term operation, ADRC has the smallest swing, indicating the most stable. The transient response of ILC is the best, and the fastest settling time reaches the 150 ms level.

4) Statistical Indication: ILC demonstrates a comprehensive improvement in the two key indicators of settling time and overshoot for the mode reversal.

In order to intuitively reflect the performance of the three controllers, the results for every 30 min within 5 h are averaged as shown in Table I. In terms of overshoot performance, ADRC is significantly better than PI. This is because ESO makes reasonable observations of the unknown part of the model and external disturbances, and realizes quick feedback in the control input $\boldsymbol{u}$. As expected, owing to the periodic iterative learning optimization, ILC limits the average overshoot to less than 1 mv. Compared with ADRC, the performance can be improved by up to 89%, and PID can be improved by more than 90%.

TABLE I
INDICATORS FOR LONG-TERM TESTING

Algorithm	Index	X Mode		Y Mode	
		UP	DOWN	UP	DOWN
PID	Overshoot (mv)	7.6	-6.9	7.5	-6.3
	Set Time (ms)	330.8	341.8	399.6	393.8
ADRC	Overshoot (mv)	8.2	-7.5	7.1	-6.0
	Set Time (ms)	393.4	383.1	442.1	456.1
ILC	Overshoot (mv)	0.8	-0.8	0.7	-0.6
	Set Time (ms)	160.5	207.4	208.8	220.8

As for settling time, the average value of the x mode ring up operation under the ILC algorithm reached 160 ms, demonstrating the fastest settling time. The proposed ILC uses historical operation data to compensate for this iteration with causal and noncausal control, and theoretically can achieve the most extreme ring up response. From the results, compared with the other two methods, the settling time of ILC can be increased by up to 59.2%. The reversal speed can be improved by up to 145%.

5) Discussions: In terms of performance in all aspects, ILC performs best in the fast mode reverse gyro. These results and reasons of the three controllers can be explained as follows:

First of all, PID treats CVG as a black box system, only considering the relationship between input and output, and cannot do anything about the potential problems. When the gyro is initialized, reason performance can be achieved by fine tuning the controller parameters. In the long-term operation, however, the reliability of PID fluctuates most obviously. This is because the plant parameters vary over time, and the effect of the initial controller parameters is getting worse.

Second, ADRC regards the gyro as a cascade integral plant, the nonlinear term caused by excessive electrostatic force can be observed by ESO as model uncertainty, and the vibration mode coupling and time-varying issues can be observed as external disturbances. At the beginning of the experiment, parameters such as the controller bandwidth and observer bandwidth are appropriately specified, and the long-term performance of the ADRC can be guaranteed to a certain extent.

Finally, ILC constantly updated with the mode reversal operation. As long as the conditions are satisfied, iterative learning can eventually converge. Compared to the two time-domain feedback algorithms, the proposed ILC scheme can provide noncausal control to cope with coupling and nonlinearity with model uncertainties through well tuned Δt and K_f. In this way, the problems can be corrected in advance to speed up the gyro mode switching. In practical gyro applications, time-varying factors such as environmental changes are slow. By continuous iterative learning, ILC can cope with the challenges of gyro parameters change through low enough T in the long-term operation process.

VI. Conclusion

In this article, an ultrafast switching control scheme is proposed and demonstrated for the CVGs to overcome the inherent limitations of mode reversal operation. A detailed investigation and description of the dynamics modeling and the working principle of the mode reversal gyro are presented at first. Theoretical analysis and experimental verification on the strong nonlinearity, mode coupling, and time-varying characteristics involved in mode reversal are conducted. A prototype control system is developed and fully verified with the proposed ILC law that demonstrated the state-of-the-art result that reached the level of 150 ms. Through the comparison of the 5-h measurement experiment, ILC has a remarkable advantage over the other two popular control algorithms in the mode reversal gyro. The results exhibit up to 145% improvement in reversal speed and 90% reduction in overshoot when compared to either PID or ADRC. It is believed that high-end navigation applications can benefit from the improved performance brought by applying the proposed advanced control technique to CVGs.

References

[1] D. Kang, C. Jang, and F. C. Park, "Unscented Kalman filtering for simultaneous estimation of attitude and gyroscope bias," *IEEE/ASME Trans. Mechatronics*, vol. 24, no. 1, pp. 350–360, Feb. 2019.

[2] L. Zacchini, V. Calabrò, M. Candeloro, F. Fanelli, A. Ridolfi, and F. Dukan, "Novel noncontinuous carouseling approaches for MEMS-Based north seeking using Kalman filter: Theory, simulations, and preliminary experimental evaluation," *IEEE/ASME Trans. Mechatronics*, vol. 25, no. 5, pp. 2437–2448, Oct. 2020.

[3] X. Zhou *et al.*, "Decaying time constant enhanced MEMS disk resonator for high precision gyroscopic application," *IEEE/ASME Trans. Mechatronics*, vol. 23, no. 1, pp. 452–458, Feb. 2018.

[4] Q. Yuan, E. Asadi, Q. Lu, G. Yang, and I.-M. Chen, "Uncertainty-based IMU orientation tracking algorithm for dynamic motions," *IEEE/ASME Trans. Mechatronics*, vol. 24, no. 2, pp. 872–882, Apr. 2019.

[5] W. Zhao, Y. Rong, C. Li, Y. Wang, X. Cai, and X. Yu, "High precision hemispherical resonator gyroscopes with oven control systems," *IEEE Sensors J.*, vol. 21, no. 6, pp. 7388–7401, Mar. 2021.

[6] C. Li *et al.*, "An FPGA-based interface system for high frequency bulk-acoustic-wave (BAW) micro-gyroscopes with in-run automatic mode-matching," *IEEE Trans. Instrum. Meas.*, vol. 69, no. 4, pp. 1783–1793, Apr. 2020.

[7] Q. Li *et al.*, "Nonlinearity reduction in disk resonator gyroscopes based on the vibration amplification effect," *IEEE Trans. Ind. Electron.*, vol. 67, no. 8, pp. 6946–6954, Aug. 2020.

[8] Y. Wang, R. Cao, C. Li, and R. N. Dean, "Concepts, roadmaps and challenges of ovenized MEMS gyroscopes: A review," *IEEE Sensors J.*, vol. 21, no. 1, pp. 92–119, Jan. 2021.

[9] X. Shao, Y. Shi, W. Zhang, and H. Cao, "Neurodynamic approximation-based quantized control with improved transient performances for MEMS gyroscopes: Theory and experimental results," *IEEE Trans. Ind. Electron.*, vol. 68, no. 10, pp. 9972–9983, Oct. 2021.

[10] F. S. Wyse and R. E. Stewart, "Vibratory gyro bias error cancellation using mode reversal," U.S. Patent 8 561 466, Oct. 22, 2013.

[11] F. S. Wyse and D. D. Lynch, "Vibrating mass gyroscope and method for minimizing bias errors therein," U.S. Patent 7 188 523, Mar. 13, 2007.

[12] C. A. Lee, "Self-calibration for an inertial instrument based on real time bias estimator," U.S. Patent 7 103 477, Sep. 5, 2006.

[13] D. M. Rozelle, "Self calibrating gyroscope system," U.S. Patent 7 912 664, Mar. 22, 2011.

[14] B. E. Boser, M. H. Kline, I. Izyumin, Y.-C. Yeh, and B. Eminoglu, "Continuous mode reversal for rejecting drift in gyroscopes," U.S. Patent 9 846 055, Dec. 19, 2017.

[15] M. H. Kline *et al.*, "MEMS gyroscope bias drift cancellation using continuous-time mode reversal," in *Proc. Transducers Eurosensors: 17th Int. Conf. Solid-State Sensors, Actuators Microsyst.*, 2013, pp. 1855–1858.

[16] H. Gu, B. Zhao, H. Zhou, X. Liu, and W. Su, "MEMS gyroscope bias drift self-calibration based on noise-suppressed mode reversal," *Micromachines (Basel)*, vol. 10, no. 12, pp. 1–17, 2019.

[17] M. Marx, S. Rombach, S. Nessler, D. De Dorigo, and Y. Manoli, "A 141-μW high-voltage MEMS gyroscope drive interface circuit based on flying capacitors," *IEEE J. Solid-State Circuits*, vol. 54, no. 2, pp. 511–523, Feb. 2019.

[18] H. Chen, Y. Zhong, and Z. Meng, "A practical PLL-based drive circuit with ultra-low-noise TIA for MEMS gyroscope," *Chin. J. Sci. Instrum., (English Edition)*, vol. 4, no. 3, pp. 7–13, 2017.

[19] Y. Su, P. Xu, G. Han, C. Si, J. Ning, and F. Yang, "The characteristics and locking process of nonlinear MEMS gyroscopes," *Micromachines*, vol. 11, no. 2, pp. 1–14, 2020.

[20] Z. Hu and B. Gallacher, "A mode-matched force-rebalance control for a MEMS vibratory gyroscope," *Sensors Actuators A: Phys.*, vol. 273, pp. 1–11, 2018.

[21] N. Nikooienejad, M. Maroufi, and S. O. R. Moheimani, "Iterative learning control for video-rate atomic force microscopy," *IEEE/ASME Trans. Mechatronics*, vol. 26, no. 4, pp. 2127–2138, Aug. 2021.

[22] J. Li, Y. Wang, Y. Li, and W. Luo, "Reference trajectory modification based on spatial iterative learning for contour control of two-axis NC systems," *IEEE/ASME Trans. Mechatronics*, vol. 25, no. 3, pp. 1266–1275, Jun. 2020.

[23] A. H. Nayfeh, *Introduction to Perturbation Techniques*. Hoboken, NJ, USA:Wiley, 1993.

[24] R. Chi, Y. Hui, C.-J. Chien, B. Huang, and Z. Hou, "Convergence analysis of sampled-data ILC for locally Lipschitz continuous nonlinear nonaffine systems with nonrepetitive uncertainties," *IEEE Trans. Autom. Control*, vol. 66, no. 7, pp. 3347–3354, Jul. 2021.

[25] Z. Bien and J.-X. Xu, *Iterative Learning Control: Analysis, Design, Integration and Applications*. New York, NY, USA: Springer-Verlag, 1998.

[26] D. A. Bristow, M. Tharayil, and A. G. Alleyne, "A survey of iterative learning control," *IEEE Control Syst. Mag.*, vol. 26, no. 3, pp. 96–114, Jun. 2006.

[27] H. Wang, X. Wang, and J. Xie, "First-order linear mechatronics model for closed-loop MEMS disk resonator gyroscope," *Sensors*, vol. 20, no. 22, 2020, Art. no. 6455.

[28] H. Cao *et al.*, "Pole-zero temperature compensation circuit design and experiment for dual-mass MEMS gyroscope bandwidth expansion," *IEEE/ASME Trans. Mechatronics*, vol. 24, no. 2, pp. 677–688, Apr. 2019.

[29] H. Li, L. Cheng, Z. Li, and W. Xue, "Active disturbance rejection control for a fluid-driven hand rehabilitation device," *IEEE/ASME Trans. Mechatronics*, vol. 26, no. 2, pp. 841–853, Apr. 2021.

[30] T. A. Khaled, O. Akhrif, and I. A. Bonev, "Dynamic path correction of an industrial robot using a distance sensor and an ADRC controller," *IEEE/ASME Trans. Mechatronics*, vol. 26, no. 3, pp. 1646–1656, Jun. 2021.

Yuchen Wang (Member, IEEE) received the B.E. degree in automation from the National Scholarship, Qingdao University of Science and Technology, Qingdao, China, in 2019. He is currently working toward the M.E. degree in Control Theory and Control Engineering with the Ocean University of China, Qingdao, China, with the National Scholarship.

He is the author of more than ten patents. His research interests include MEMS, resonator interface electronics, measurement and control systems, and calibration and compensation technology.

Jiakun Hou received the B.E. degree in automation from the Ocean University of China, Qingdao, China, in 2019 where he is currently working toward the M.E. degree in control engineering.

His research interests include MEMS interface electronics, measurement and control systems, and signal processing.

Chong Li (Member, IEEE) received the B.E. degree in automation and M.E. degree in control theory and control engineering from the Ocean University of China, Qingdao, China, in 2009 and 2012, respectively, and the Ph.D. degree in mechanical engineering from Auburn University, Auburn, AL, USA, in 2016.

He was a Postdoctoral Research Fellow with the Integrated MEMS Laboratory (IMEMS), Center for MEMS and Microsystems Technologies (CMMT), Georgia Tech, Atlanta, GA, USA, from 2016 to 2018. He is currently an Associate Professor with the Department of Automation and Measurement, Ocean University of China. His research interests include MEMS, control systems, high-performance computing, machine learning, and artificial intelligence.

Jin Wu (Member, IEEE) was born in May 1994 in Zhenjiang, China. He received the B.S. degree from the University of Electronic Science and Technology of China, Chengdu, China. He is currently working toward the Ph.D. degree with Hong Kong University of Science and Technology, Hong Kong.

Since 2018, he has been a Research Assistant with the Department of Electronic and Computer Engineering, Hong Kong University of Science and Technology. He was with Tencent Robotics X, Shenzhen, China, from 2019 to 2020. During 2012 to 2018, he was in the UAV industry and has brought up two companies.

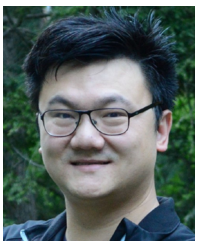

Yu Jiang (Member, IEEE) received the B.Sc. degree in applied mathematics from Sun Yat-sen University, Guangzhou, China, in 2006, the M.Sc. degree in automation science and engineering from the South China University of Technology, Guangzhou, China, in 2009, and the Ph.D. degree in electrical engineering from New York University, New York, NY, USA, in 2014.

Currently, he is the Principle Scientist with ClearMotion, Billerica, MA, USA. Prior to joining the company, he worked as a Software Engineer with The MathWorks, Natick, MA, USA, and the Controls Tech Lead with ISEE AI, Cambridge, MA, USA. He is the first author of the book *Robust Adaptive Dynamic Programming* (Hoboken, NJ, USA: Wiley, 2017). His research interests include learning-based control and its applications in preview active suspension control and autonomous truck-trailer systems.

Dr. Jiang was the recipient of the Shimemura Young Author Prize (with Prof. Z.P. Jiang) at the 9th Asian Control Conference in Istanbul, Turkey, in 2013.

Ming Liu (Senior Member, IEEE) received the B.A. degree in automation from Tongji University, Shanghai, China, in 2005, and the Ph.D. degree from the Department of Mechanical and Process Engineering, ETH Zurich, Zurich, Switzerland, in 2013, supervised by Prof. Roland Siegwart.

He is currently with the Electronic and Computer Engineering, Computer Science and Engineering Department, Robotics Institute, The Hong Kong University of Science and Technology (HKUST), Hong Kong, China, as an Associate Professor. His research interests include dynamic environment modeling, deep-learning for robotics, 3-D mapping, machine learning, and visual control.

Dr. Liu is a Program Member of Robotics: Science and Systems (RSS) 2021. He is currently an Associate Editor for *IEEE Robotics and Automation Letters*, *International Journal of Robotics and Automation*, *IET Cyber-Systems and Robotics*, IEEE Intelligent Robots and Systems (IROS) Conference 2018, 2019, and 2020. He served as a Guest Editor of special issues in IEEE TRANSACTIONS ON AUTOMATION SCIENCE AND ENGINEERING.

John Y. Hung (Fellow, IEEE) received the B.S. degree in electrical engineering from The University of Tennessee, Knoxville, TN, USA, in 1979, the M.S.E. degree in electrical engineering from Princeton University, Princeton, NJ, USA, in 1981, and the Ph.D. degree in electrical engineering from the University of Illinois at Urbana-Champaign, Champaign, IL, USA, in 1989.

From 1981 to 1985, he was with Johnson Controls, Milwaukee, WI, USA, developing microprocessor-based controllers for commercial heating, ventilation, and air conditioning systems. From 1985 to 1989, he was a Consultant Engineer with Polyanalytics Inc., Knoxville, TN, USA. In 1989, he joined Auburn University, Auburn, AL, USA, where he is currently a Professor Emeritus with the Department of Electrical and Computer Engineering. He holds two U.S. patents in control systems. His teaching and research interests include nonlinear control systems and signal processing with applications in process control, robotics, electric machinery, and power electronics.

Dr. Hung was the President of the IEEE Industrial Electronics Society, in 2014 and 2015, respectively. He received several awards for his teaching and research, including the Best Paper Awards from the IEEE TRANSACTIONS ON INDUSTRIAL ELECTRONICS and IEEE *Industrial Electronics Magazine*. He served as an Associate Editor for the IEEE TRANSACTIONS ON INDUSTRIAL ELECTRONICS, from 1996 to 2005, and the IEEE TRANSACTIONS ON CONTROL SYSTEMS TECHNOLOGY, in 1997 and 1998. He served on the IEEE Board of Directors in 2017 and 2018.